Zeitschrift: Helvetica Physica Acta
Band: 60 (1987)
Heft: 7

Artikel: Numerical simulation of eutectic solidification in the laser treatment of materials
Autor: Rappaz, M. / Carrupt, B. / Zimmermann, M.
DOI: https://doi.org/10.5169/seals-115877

Helvetica Physica Acta, Vol. **60** (1987) 924–936

0018–0238/87/070924–13$1.50 + 0.20/0

Numerical simulation of eutectic solidification in the laser treatment of materials[1])

By M. Rappaz, B. Carrupt, M. Zimmermann and W. Kurz

Laboratoire de métallurgie physique
Ecole Polytechnique Fédérale de Lausanne
34, ch. de Bellerive, CH-1007 Lausanne, Switzerland

In honor of Prof. B. Vittoz 60th birthday

(16. VII. 1987)

Summary. An upwind finite difference program has been written in order to simulate the stationary shape of the liquid pool which forms under a high-power laser beam moving at constant velocity over a surface. The model considers 3-dimensional heat-diffusion and uses an enthalpy formulation. That is, the volumic enthalpy, H, which is the sum of the specific heat and of the latent heat contributions, is considered to be the variable. The eutectic plateau of the temperature function, $T(H)$, which is supposed to occur at the equilibrium eutectic temperature, T_E, is treated using Newton–Raphson iteration. After finding the temperature field with a Gauss–Seidel method, the position of the eutectic interface is calculated. Considering a longitudinal section of the melt pool, the temperature gradient and the solidification rate are deduced at each point of the resolidifying part of this interface. From these values, the undercooling of the front and the eutectic spacing are computed as a function of the depth of the heat-treated surface, using a recently developed theory of the rapid solidification of eutectics. The results obtained from this micro-macroscopic coupling are discussed and compared with experimental observations made on Al–Cu alloys.

1. Introduction

The surface treatment of materials by laser is of great interest in many technical applications. By moving a high-power beam, such as that produced by a CO_2 laser, over a surface (see Fig. 1) very fast heat-treatment or rapid melting-solidification of the base material can be obtained at depths varying from a few microns to several millimeters. During laser remelting, the rate of solidification governs the possible appearance of metastable phases, their composition, and the scale of the microstructure [1, 2].

When a stationary regime is reached, the solidification rate, v_s, at any point of the interface can be directly deduced from the shape of the melt pool. As indicated in Fig. 1, $v_s = v_b \cdot \cos\theta$, where θ is the angle between the normal to the interface and the traverse velocity, v_b, of the laser beam [3]. Therefore, in order

[1]) This project is supported by the Commission pour l'Encouragement de la Recherche Scientifique, Switzerland.

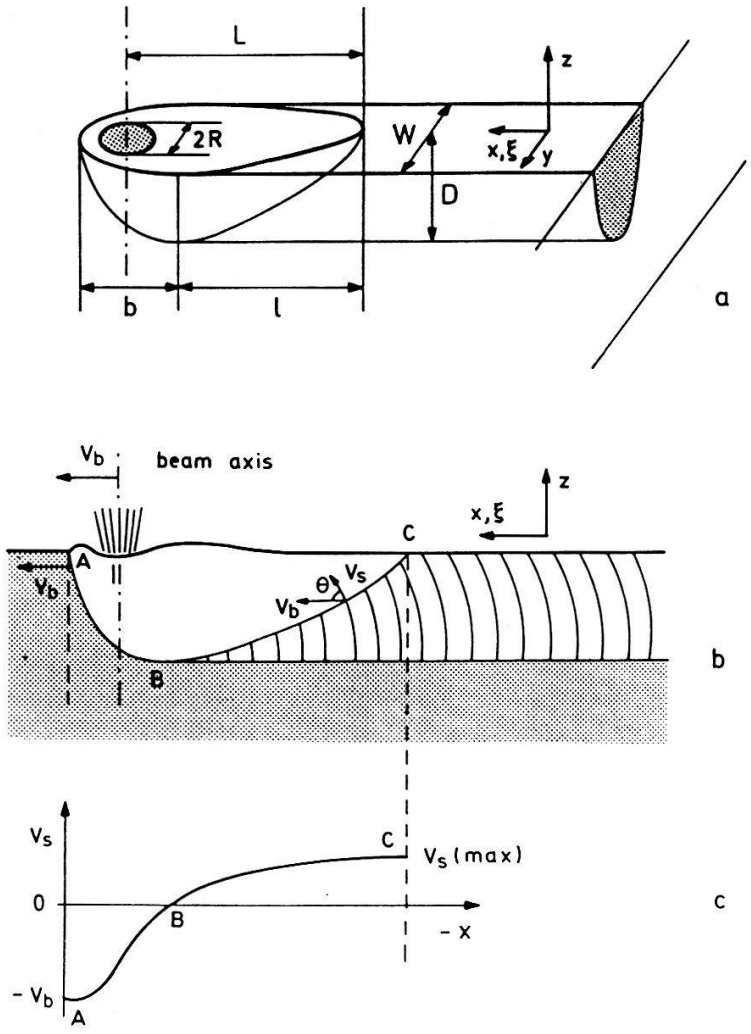

Figure 1
Shape of the melt pool during continuous laser remelting. a) geometry at high beam velocities; b) longitudinal section through trace; c) solid–liquid interface rate as a function of distance, x.

to control the composition and the microstructural scale of the laser-treated surface, it is essential to control the shape of the melt pool.

Since it is difficult to deduce this shape from experimental observations, numerical simulation is a very useful tool for assessing the influence of the various parameters which affect the process. Furthermore it is essential for a close process control. It has already been applied to related topics such as laser heat-treatment and arc-, laser- or electron beam-welding [4–6]. However, they are usually limited to low traverse speeds and no upwind procedure has been used in the numerical calculations. Furthermore, these authors did not consider the complex phenomena of microstructure formation and the high undercooling of the front which is associated with a high solidification rate [1].

The aim of the present paper is to simulate the laser remelting/resolidification of eutectic alloys at high rate. For this purpose, the temperature field is computed from the stationary heat-diffusion equation using a finite difference method (FDM). The latent heat release which is associated with the

phase transformation is assumed to occur at the equilibrium temperature, T_E. Based upon an enthalpy formulation [7], the FDM solution is obtained using an upwind procedure [8]. From the macroscopic calculation of the heat-flow, the shape of the equilibrium eutectic front is deduced, together with the solidification rate, v_s, and the mean thermal gradient, G, at each point of this interface. Knowing these values, the eutectic spacing, λ_E, and the undercooling, ΔT_E, can be calculated using a recently developed theory of eutectic growth at high solidification rates [1]. Although the macroscopic calculation of the heat flow should be reiterated using the deduced undercooling, a first-step iteration already provides valuable information concerning the shape of the interface and the microstructural parameters. The results are discussed in the light of recent experimental investigations of Al–Cu eutectic alloys.

2. Macroscopic model

2.1. *Physical model*

Using an enthalpy formulation [7], the stationary heat-diffusion equation corresponding to the laser process shown in Fig. 1 can be written as:

$$\operatorname{div}(k(T) \cdot \operatorname{grad} T(\mathbf{r})) + v_b \cdot \frac{\partial H}{\partial \xi} = 0 \tag{1}$$

where k is the temperature-dependent thermal conductivity and $T(\mathbf{r})$ is the temperature field measured in a reference frame, $O\xi yz$, moving with the laser, where the ξ-direction coincides with the velocity, v_b, of the laser beam. The enthalpy, H, of a eutectic alloy is related to its temperature through the relationship:

$$H(T) = \int_0^T c_p(T') \cdot dT' + L \cdot u(T - T_e) \tag{2}$$

where $c_p(T)$ and L are the volumic specific heat and latent heat, respectively, u is the Heaviside function, and T_e is the equilibrium eutectic temperature.

Equation 1 is solved within a volume, Ω, of the laser-treated material which can be chosen arbitrarily (see Fig. 2). However, Ω must be large with respect to the size of the laser beam and to that of the melt pool, so that the boundary condition at the surface, Γ_1, within the metal can be fixed without ambiguity. For that reason, the size of Ω is chosen so as to obtain temperatures on Γ_1 which are close to the initial temperature of the base material. More precisely, the boundary condition at Γ_1 is deduced from a point-source model [9], which, for 3-dimensions, gives:

$$T(\xi, r) = \frac{\beta P}{2\pi k r} \exp\left\{\frac{-v_b \cdot (\xi + r)}{2a}\right\} \qquad (\xi, r) \in \Gamma_1 \tag{3}$$

where P the total power of the point heat-source, β is the absorption coefficient,

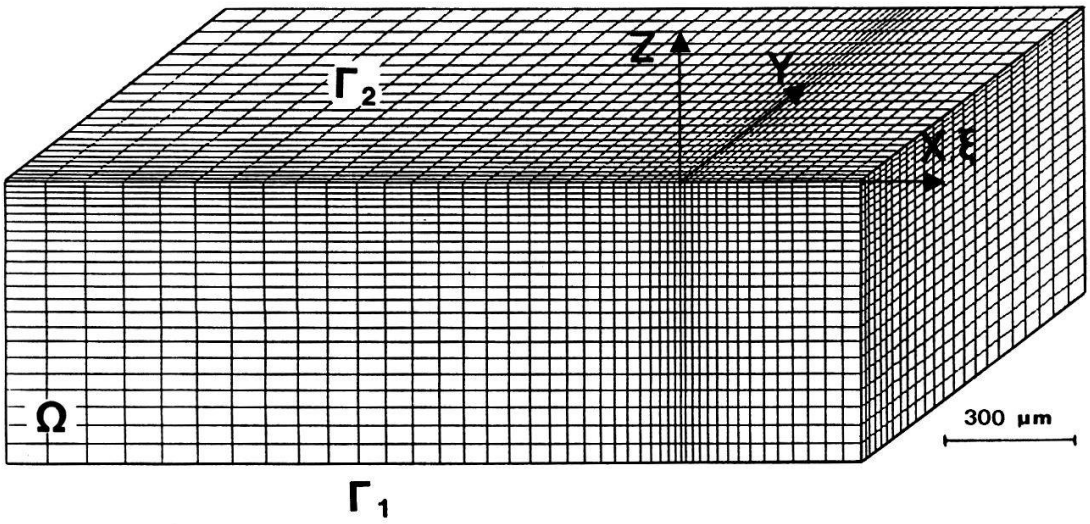

Figure 2
Mesh used for the numerical calculations. At the free surface, Γ_2, a heat-flow balance is imposed while, within the internal boundary, Γ_1, the temperature is set to a value given by a point-source model.

and a is the thermal diffusivity (i.e. $a = k/c_p$). The radius is simply given by:

$$r = \sqrt{\xi^2 + y^2 + z^2}$$

At the free surface Γ_2, the boundary condition is given by:

$$k \cdot \frac{\delta T}{\delta z}(\xi, y, 0) = q(\xi, y) + h \cdot (T(\xi, y, 0) - T_a) \tag{4}$$

h is the coefficient of heat transfer between the surface of the material (temperature = $T(\xi, y, 0)$) and the ambient temperature (T_a). The energy distribution profile, $q(\xi, y)$, which effectively heats the material is related to P (equation 3) by the relationship:

$$\beta P = \int_{-\infty}^{+\infty} dy \int_{-\infty}^{+\infty} q(\xi, y)\, d\xi \tag{5}$$

2.2. *Numerical formulation*

Equation (1) is solved using a FDM scheme with a mesh which is similar to that shown in Fig. 2. It typically contains 25920 nodes ($45 \times 24 \times 24$ mesh points in the ξ-, y- and z-directions, respectively). As can be seen, the mesh size is adapted to the thermal gradients since it is refined in the region close to the laser beam. Considering a grid point, C, within the volume, Ω, and its 6 neighbours (see Fig. 3), equation (1) can be integrated over the volume, $\Delta x\, \Delta y\, \Delta z$, of the mesh.

Using the divergence theorem and integrating $(\partial H/\partial \xi) \cdot d\xi$, the following relationship is obtained:

$$\int_{\Gamma_c} k(T) \cdot \mathbf{grad}\, T \cdot \mathbf{n} \cdot d\Gamma_c + v_b \cdot \int_{\Delta y} dy \int_{\Delta z} dz \cdot [H_R - H_L] = 0 \tag{6}$$

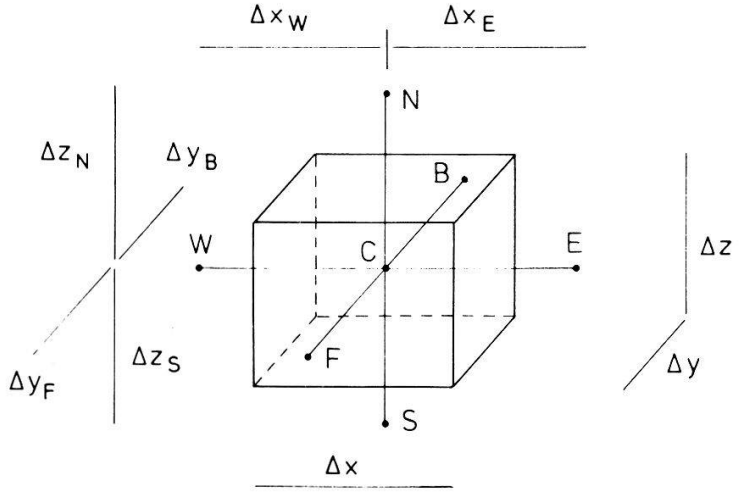

Figure 3 Internal grid point, C.

where $\mathbf{n}$ is the unit vector normal to the surface Γ_c, H_R and H_L represent the average enthalpy at the right and left of C, respectively. Introducing an upwind parameter, α, the enthalpy difference in equation (6) can be written as:

$$v_b \cdot \int_{\Delta y} dy \int_{\Delta z} dz \cdot [H_R - H_L] = v_b \cdot \Delta y \Delta z \cdot [H_E\alpha + H_C(1-2\alpha) + H_W(\alpha - 1)] \tag{7}$$

with $\frac{1}{2} \leq \alpha \leq 1$

Using equation (7), equation (6) becomes:

$$\begin{aligned} &k_{EC}\frac{\Delta y\,\Delta z}{\Delta x_E}(T_E - T_C) + k_{WC}\frac{\Delta y\,\Delta z}{\Delta x_W}(T_W - T_C) \\ &+ k_{NC}\frac{\Delta x\,\Delta y}{\Delta z_N}(T_N - T_C) + k_{SC}\frac{\Delta x\,\Delta y}{\Delta z_S}(T_S - T_C) \\ &+ k_{FC}\frac{\Delta x\,\Delta y}{\Delta y_F}(T_F - T_C) + k_{BC}\frac{\Delta x\,\Delta z}{\Delta y_B}(T_B - T_C) \\ &+ v_b \cdot \Delta y \cdot \Delta z \cdot [H_E\alpha + H_C(1-2\alpha) + H_W(\alpha - 1)] = 0 \end{aligned} \tag{8}$$

The thermal conductivities appearing in equation (8), k_{ic} with $i = E, W, N, S, B, F$, correspond to $k(T_{ic})$ taken at the mid-temperature, $T_{ic} = (T_i + T_c)/2$.

Following Thomasset [8], a stable and accurate scheme can be obtained for the linear case, i.e. when $H(T) = c_p T$, with:

$$\alpha = \frac{1}{2}\left[1 + \coth\left(\frac{\gamma}{2}\right)\right] - \frac{1}{\gamma} \quad \text{with} \quad \gamma = \frac{v_b \cdot \Delta x}{k/c_p} \tag{9}$$

Taking into account the boundary conditions for the nodes of $\Gamma_1 \cup \Gamma_2$, the final equation below is obtained:

$$[k] \cdot \mathbf{T} + [v_b] \cdot \mathbf{H} = \mathbf{bc} \tag{10}$$

with

$[k]$: conductivity matrix
$[v_b]$: matrix of the advection term
$\mathbf{T}, \mathbf{H}$: vectors of temperatures and enthalpies at the nodes
$\mathbf{bc}$: vector of the boundary conditions

Equation (10) is solved using a Newton–Raphson iteration method, where the enthalpy is the variable rather than the temperature. The enthalpies at the $(p+1)$th iteration, $\mathbf{H}^{(p+1)}$, are deduced from the temperatures and the enthalpies at the (p)th iteration according to:

$$[A]^{(p)} \cdot \mathbf{H}^{(p+1)} = \mathbf{b}^{(p)} \tag{11}$$

with:

$$[A]^{(p)} = [k]^{(p)} \cdot \left[\frac{\partial T}{\partial H}\right]^{(p)} + [v_b] \tag{12}$$

$$\mathbf{b}^{(p)} = \mathbf{bc}^{(p)} - [k]^{(p)} \cdot \left(\mathbf{T}^{(p)} - \left[\frac{\partial T}{\partial H}\right]^{(p)} \cdot \mathbf{H}^{(p)}\right) \tag{13}$$

The components of the diagonal matrix, $\left[\frac{\partial T}{\partial H}\right]^{(p)}$, are the derivatives of the function $T(H)$ taken at the enthalpies, $\mathbf{H}^{(p)}$. Since the conductivity matrix, $[k]$, is normally only slightly dependent upon T, it is updated at each iteration instead of being linearised. As the conductivity and the advection matrices, $[k]$ and $[v_b]$, have only 7 and 3 non-zero diagonals, respectively, a Gauss-Seidel iteration method was used to solve Equation 11 at each iteration (p). This solution technique minimizes the computer memory space required for the calculations and can be easily vectorized for parallel processing.

3. Microscopic model

Jackson and Hunt [10] have proposed models for lamellar and fibrous eutectic growth. However, in order to solve the diffusion equation, they make two assumptions which are no longer valid under rapid solidification conditions. These simplifications are: 1) the eutectic structure grows at small Péclet numbers, i.e. $P \equiv \lambda v_s / 2D \ll 1$, where λ is the eutectic interphase spacing, v_s is the solid – liquid interface growth rate, and D is the diffusion coefficient of solute in the liquid; 2) the liquid composition at the eutectic solid – liquid interface is close to the eutectic composition.

Trivedi, Magnin and Kurz [1] have relaxed these assumptions and discussed lamellar eutectic growth at high growth rates ($P > 1$). They show that one of the fundamental results of the theory of diffusional phase transformations, i.e.

$$\lambda^2 v_s = \text{const.} \tag{14}$$

is no longer true. Instead, when $P > 1$, $\lambda^2 v_s$ increases sharply, producing coarser

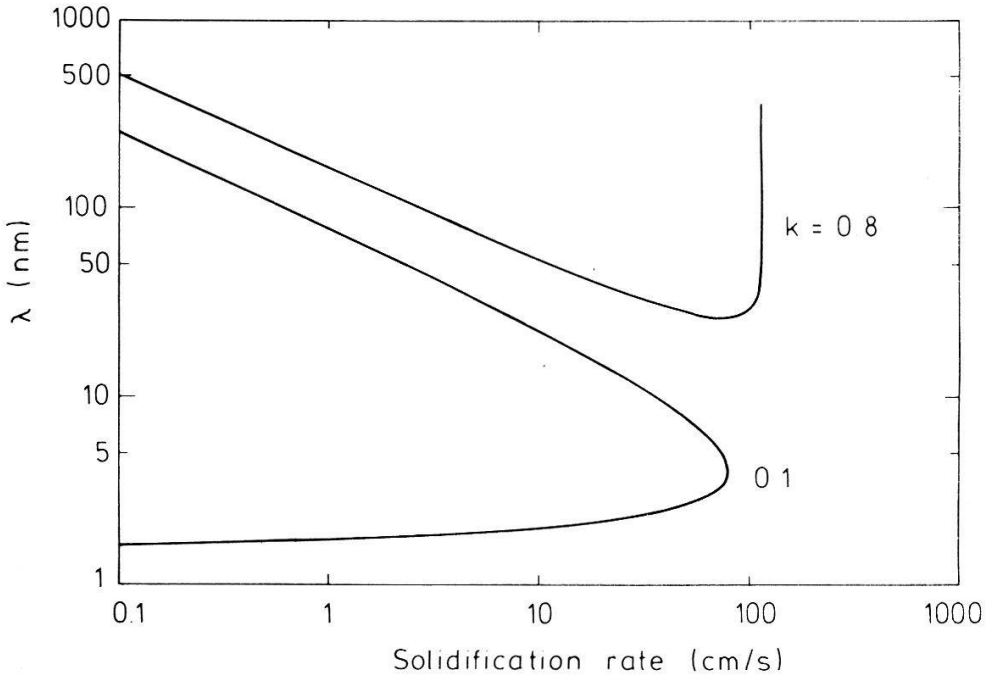

Figure 4
Interlamellar spacing, λ, versus solidification rate, v_s, of Al–Cu eutectic alloy for two different values of the partition coefficient, k.

microstructures at higher rates. Figure 4 illustrates such a behaviour when $k \rightarrow 1$. The distribution coefficient k is the ratio of the composition of the solid to the composition of the liquid at the interface and is assumed to be constant. When k (or the solubility of the solid phases) is very small, solute rejection at the growth front becomes large and the interface temperature falls sharply. In such a case, the temperature dependence of the diffusion coefficient, $D(T)$, will have an effect. A high undercooling below the equilibrium temperature will retard the transformation, due to the small D-value. This is the reason for the bending back of the $\lambda(v_s)$ curve for $k = 0.1$ in Fig. 4.

Figure 5 shows the corresponding interface temperature versus growth rate relationship. One can see that, for large k-values, the diffusion coefficient has only a small effect while, for small k, a pronounced D-dependent maximum in the growth rate exists.

The maximum rate of eutectic growth for the various k-values is always of the same order of magnitude and, in the case of the Al–Cu system examined here, is about 1 m/s. (This limit also corresponds closely to the limit of absolute stability of dendritic growth [2]).

Knowing the change with growth rate of the interface temperature and of the eutectic interphase spacing, the microstructural scale across the remelted zone can be deduced by combining the prediction of the microscopic model with the isotherm displacement rates. (Here the temperature gradient does not have a direct influence upon the eutectic growth).

The microscopic parameters used in the following section when coupling the macroscopic calculations of heat flow with the mechanisms of eutectic growth are listed in Table 1.

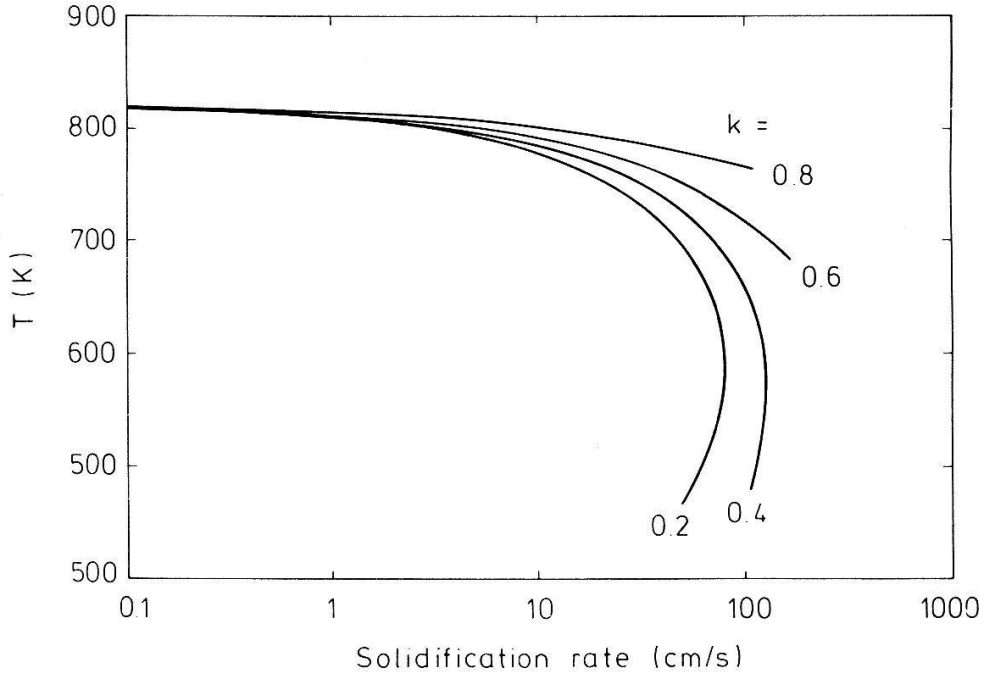

Figure 5
Temperature at the solidification front, T, versus solidification rate, v_s, of Al–Cu eutectic alloy for different values of the partition coefficient, k.

4. Results

Figure 6 shows a 3-dimensional view of the isotherms deduced from the macroscopic model described in Section 2. The corresponding experimental parameters as well as the conditions used in the FDM calculations, are given in Table 2. The temperature values corresponding to the various isotherms are listed in the figure caption. The liquid pool is outlined by the first isotherm, $T = 550°C$. (It should be recalled that the solid – liquid phase transition was supposed to occur at the equilibrium eutectic temperature, without including any undercooling in the macroscopic heat-flow calculations.) The result shown in Fig. 6 was then used to predict microstructural features within the longitudinal section (i.e.

Table 1
Physical constants assumed for microscopic calculations of the Al–Cu system

Eutectic composition	33.2 wt%
Eutectic temperature	821 K
Volumic fraction of the α-phase	0.55
Equilibrium partition coefficient	0.17
Eutectic tie line	46.9 wt%
Liquidus slope of the α-phase	−4.6 K/wt%
Liquidus slope of the β-phase	4.8 K/wt%
Preexponential constant, D_0	1.05 ± 0.15 cm^2/s [11]
Activation energy for diffusion	23.8 ± 1.3 kJ/mol [11]
Capillarity constant	$2.6 \cdot 10^{-6}$ cm · wt%

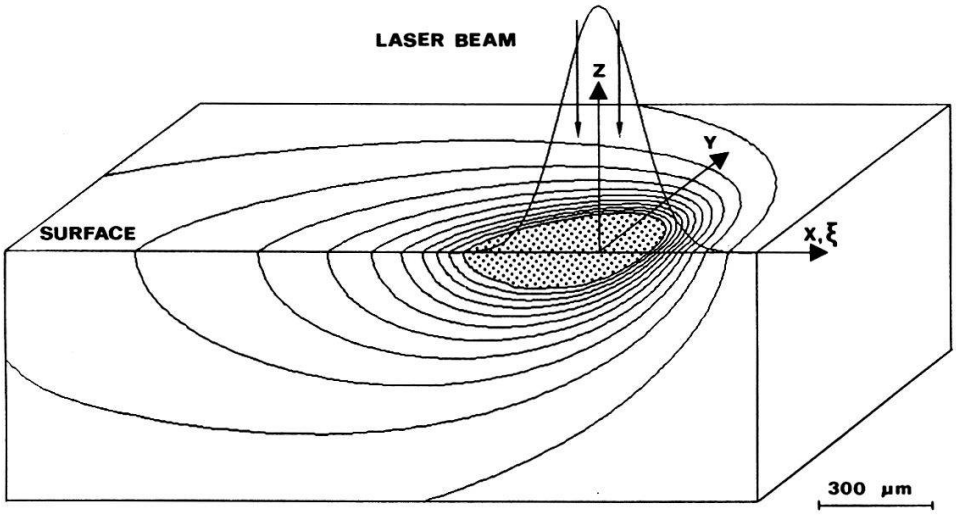

Figure 6
Three-dimensional view of the isotherms as calculated using the conditions listed in Table 2. The liquid pool (shadowed area) is outlined by the first isotherm $T = 550°C$. Other isotherms correspond to decreasing temperatures in 50°C steps.

section parallel to the traverse direction of the laser beam and perpendicular to the surface, taken through the centre of the laser trace).

Figure 7 is an enlarged view of the eutectic isotherm of Fig. 6. Only the part of the pool behind the laser beam, i.e. the part which is solidifying, is shown. It has been smoothed using a least-square fit because the isotherm obtained from the FDM calculations exhibits fluctuations which are related to the use of the enthalpy method. From this smoothed solid – liquid interface, the solidification rate is calculated and plotted against the depth, z, of the melt pool, (see Fig. 8). The thermal gradient at each point of the interface is also shown in Fig. 8.

Combining the results shown in Figs. 4–5 for the growth of the eutectic with those obtained from the macroscopic heat-flow calculations (Fig. 8) gives the depth-dependence of the lamellar spacing and of the undercooling, shown in Fig. 9 and Fig. 10, respectively.

Table 2
Process parameters and conditions used in the FDM calculations

Process parameters	
Power of the laser beam	1.5 kW
Absorption coefficient	0.15
Traverse speed of the laser	1.0 m/s
Standard deviation of the Gaussian intensity profile of the beam	0.1 mm
Heat transfer coefficient to ambient air	100 $W/m^2/K$
Thermophysical properties of Al–Cu alloy	
Volumic latent heat of fusion	$9.5 \cdot 10^8$ J/m^3
Mean volumic specific heat	$2.7 \cdot 10^6$ $J/m^3/K$
Mean conductivity	200 W/m/K
FDM conditions	
Total number of nodes	25920
Computing time on a Cray-1s	2'40"

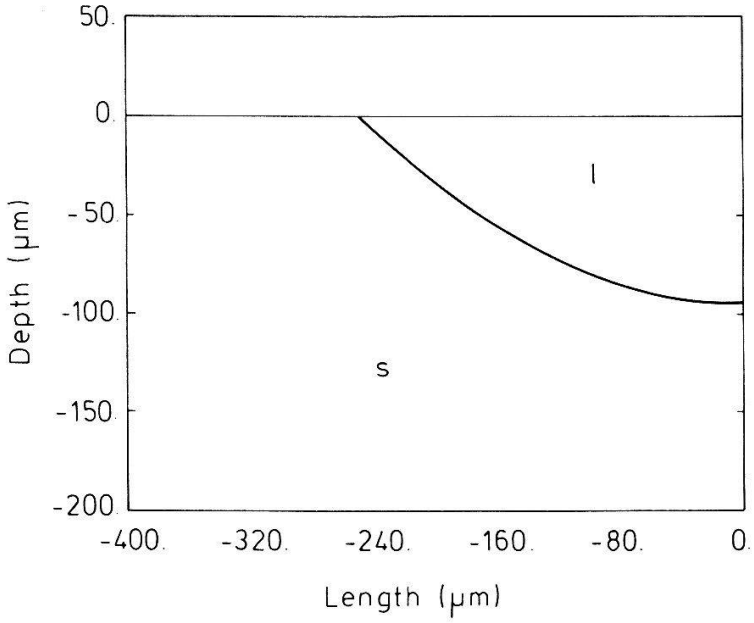

Figure 7
Enlarged view of the rear of the solid – liquid interface of Fig. 6 as calculated for the longitudinal section. This interface has been smoothed using a least-squares fit. (The position of the vertical z-axis has been moved with respect to Fig. 6 in order that it coincide with the maximum depth of the liquid pool).

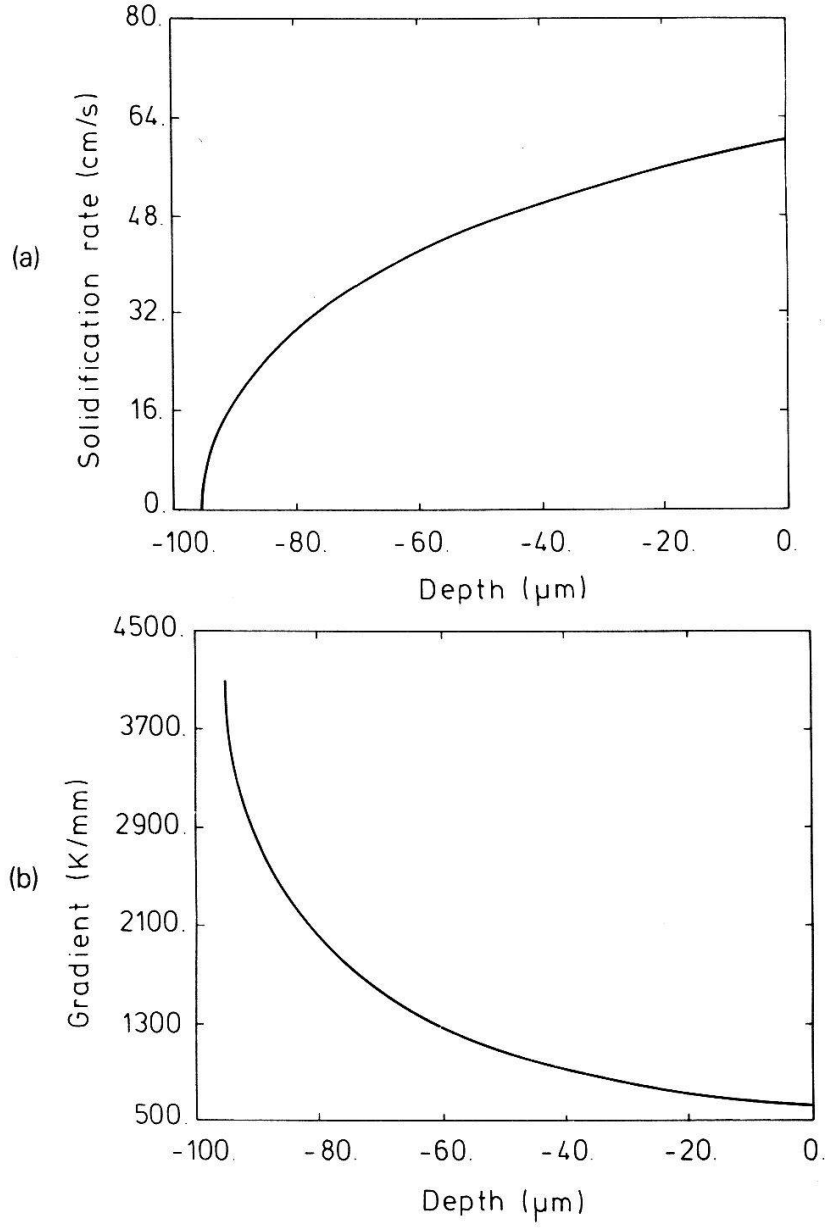

Figure 8
(a) Solidification rate, v_s, (b) thermal gradient, G, versus depth, z, of the liquid pool. These curves have been calculated from Figs. 6 and 7.

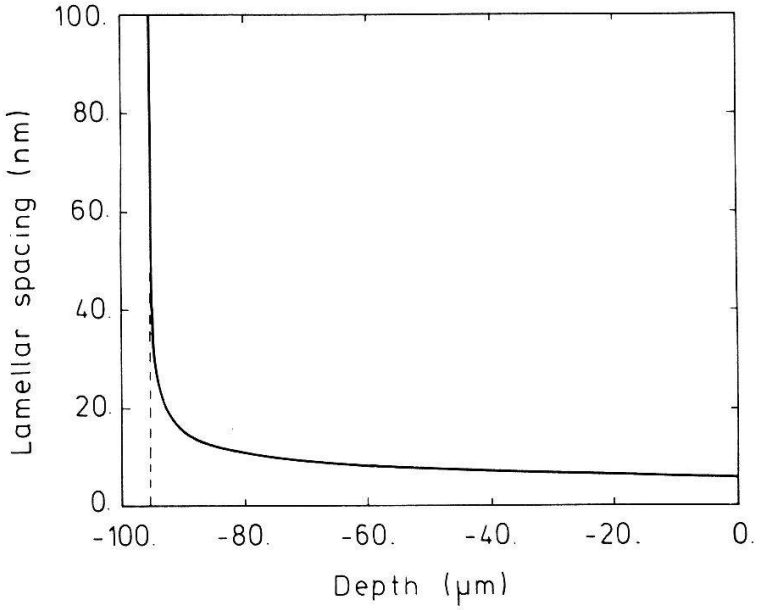

Figure 9
Interlamellar spacing, λ, versus depth, z, of the liquid pool as obtained from the results shown in Figs. 4 and 8a.

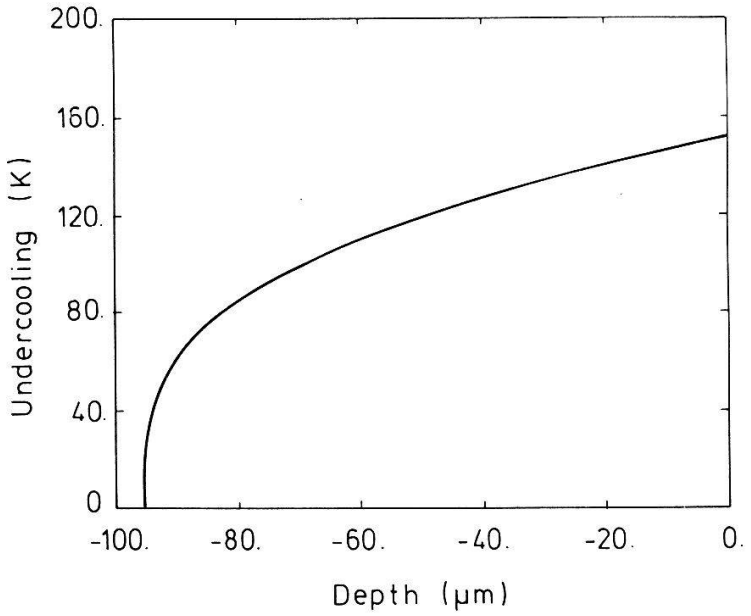

Figure 10
Undercooling ($T_e - T$) versus depth, z, of the liquid pool as obtained from the results shown in Figs. 5 and 8a.

5. Discussion

Firstly, it is interesting to note that the lamellar spacing (Fig. 9) rapidly decreases at the bottom of the pool and then becomes essentially constant. This is due to the fact that the velocity of the solidification front increases rapidly from zero at the bottom of the pool, typically as the square root of the depth. The

Jackson and Hunt model of eutectic growth, which predicts that $\lambda^2 v_s = \text{const.}$, would result in a $z^{-1/4}$ depth-dependence of the lamellar spacing.

The corresponding undercooling of the eutectic front shown in Fig. 10 also increases rapidly from the bottom of the pool. As can be seen, the largest undercooling (about 160°C) is predicted to occur at the surface of the pool, where the thermal gradients are the smallest, see Fig. 8. This depth-dependent undercooling may therefore substantially modify the shape of the melt pool. In order to account for this, an iterative coupling between the micro- and macroscopic models should be included. This is beyond the scope of the present paper.

A comparison with experimental observations is informative. Firstly, the depth of the melt pool predicted by the thermal calculations (95 μm) is in good agreement with that observed on real specimens (85 μm). This is not the case for the width of the pool on the trace of the laser beam on the top surface (calculated: 350 μm; measured: 250 μm). This discrepancy might be due to an under-estimated heat-transfer coefficient, to surface-induced convection, whose effect would be most noticeable at the free surface, to the non-gaussian energy distribution profile of the laser beam, or to a temperature-dependet absorption coefficient.

Figure 11 shows the eutectic microstructure observed by transmission electron microscopy at various depths, z, in the laser trace. While the lamellar spacing of the base material is about 1 μm, see Fig. 11a, the spacing of the eutectic which forms directly at this interface is already only 55 nm. At the mid-depth of the pool (Fig. 11b), the spacing is 13 nm. Close to the surface (Fig. 11c), the spacing (12 nm) does not differ significantly from the previous value, but the eutectic morphology is wavy. These findings correspond well to the calculated results shown in Fig. 9.

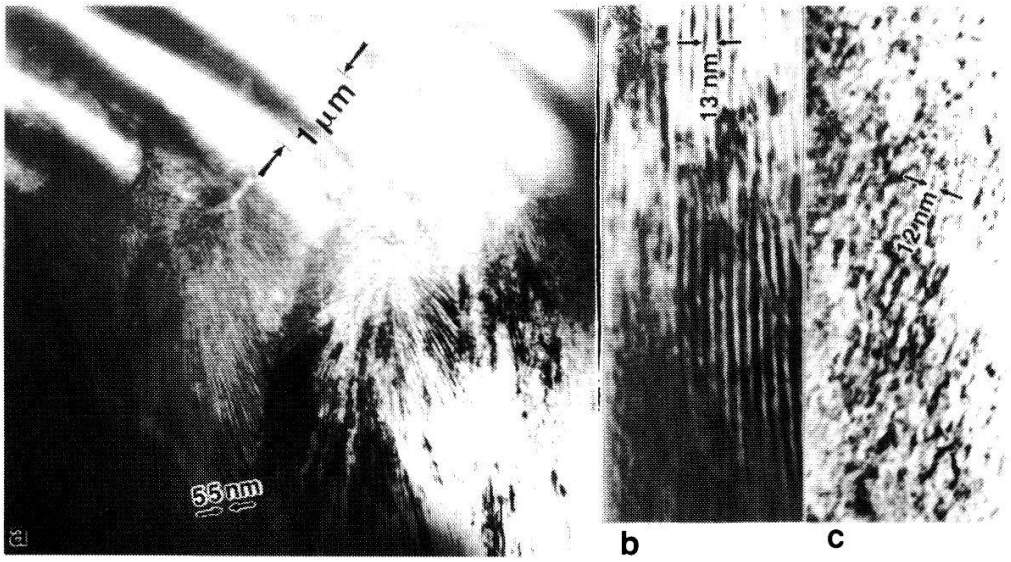

Figure 11
Transmission electron microscope micrographs of the Al–Cu eutectic alloy at various depths in the laser trace: a) Interface between the base material and the remelted zone at the bottom of the trace; b) mid-depth of the trace; c) close to the surface.

6. Conclusions

One simple laser trace corresponds to a whole range of solidification conditions. Knowing from macroscopic heat flow calculations the velocity at each point of the eutectic interface permits one to deduce the spacing versus growth rate dependence. From that point of view, the combined micro-macroscopic modelling is of great interest not only in assessing the melt pool geometry and dimensions, but also in predicting the velocity and the gradient in 3-dimensions. Such calculations will permit in the near future an on-line control of laser treated surfaces. Work is in progress to improve the predictions by taking account of convection in the pool and by incorporating the space-dependent undercooling into the enthalpy formulation.

REFERENCES

[1] R. TRIVEDI, P. MAGNIN and W. KURZ, Acta Met. *35,* (1987), p. 971.
[2] W. KURZ, B. GIOVANOLA and R. TRIVEDI, Acta Met. *34,* (1986), p. 823.
[3] M. RAPPAZ, M. GREMAUD, R. DEKUMBIS and W. KURZ, *Solidification front and growth rate during laser remelting,* First Europe Conf. Laser Treatment (ECLAT), DGM conference proceedings (Bad Nauheim, Germany, 1986).
[4] C. L. CHAN, R. ZEHR, J. MAZUMDER and M. M. CHEN, in *Modelling and control of casting and welding processes,* Eds. S. Kou and R. Mehrabian, AIME-publication, The Metallurgical Society Inc., 1986, p. 229.
[5] G. F. CAREY and R. MCLAY, in *Numerical methods in thermal problems,* Vol. IV, Eds. R. W. Lewis and K. Morgan, Pineridge Press, Swansea, UK, 1985, p. 161.
[6] S. KOU and D. K. SUN, Met. Trans. *16A,* (1985), p. 203.
[7] J.-L. DESBIOLLES, J.-J. DROUX, J. RAPPAZ and M. RAPPAZ, *Simulation of solidification of alloys by the finite element method,* to appear in Computer Physics Report (1987).
[8] F. THOMASSET, *Implementation of finite element methods for Navier–Stokes equations,* Springer-Verlag, New York, 1981.
[9] J. F. LANCASTER, *Metallurgy of Welding,* George Allen & Unwin Pub., London, 1980, p. 42.
[10] K. A. JACKSON and J. D. HUNT, Trans. AIME, *236,* (1966), p. 1129.
[11] T. EJIMA, T. YAMAMURA, N. UCHIDA, Y. MATSUZAKI and M. NIKAIDO, J. Jpn Inst. Met., *44,* (1980), p. 316.